AO-Al_2O_3-Nb_2O_5 (A=Ca,Sr,Ba) Phase Diagrams Reveal Potentially Useful Wireless Ceramic

The commercial competitiveness of next-generation base stations depends on improved resonators and filters manufactured from ceramics with better properties and/or reduced processing costs. Experimental phase equilibria and structure-property studies contribute to the fundamental understanding of these ceramics which will eventually permit the rational design of advanced ceramics with controlled dielectric performance. In addition, the existence of potentially useful phases and phase assemblages in selected oxide systems is revealed.

Dielectric oxide ceramics with high permittivity, low dielectric loss, and near-zero temperature dependence of dielectric properties are critical elements in components such as resonators, oscillators, and filters for wireless communications. Relatively few ceramic systems are currently available with the properties needed for practical applications at various operating freqencies. Tantalate-based perovskite derivatives $Ba_3MTa_2O_9$, with M= Zn or Mg, are unique in exhibiting permittivities of about 30 together with extremely low dielectric loss tangents (< 10^{-5} at 1 GHz). These studies were motivated by the need for dielectric oxides that could serve as less costly alternatives to the tantalate systems for high-frequency high-power resonator applications. Ternary Al_2O_3-Nb_2O_5-containing systems were selected because the polarizability of Ta^{5+} is intermediate between that of Al^{3+} and Nb^{5+}, and because similar crystal chemistry is expected.

Subsolidus phase equilibria in the CaO:Al_2O_3:Nb_2O_5 system at 1325 °C in air were determined. One ternary phase forms, Ca_2AlNbO_6, which exhibits a perovskite-related structure with 1:1 or NaCl-type ordering of Al^{3+} and Nb^{5+} on the B-sites. Reference X-ray powder diffraction data for this monoclinic compound were prepared. Capacitance methods at 1 MHz were used to determine the dielectric constants and associated temperature coefficients for eleven compounds in this system. The diagram shown at the right includes the resulting relative permittivity values (estimated uncertainty 10%) and the signs of their temperature coefficients. As indicated with the red line, Ca_2AlNbO_6 and $Ca_3Nb_2O_8$ co-exist in equilibria, and were found to exhibit temperature coefficients with opposite signs. Five compositions along this line were prepared and their dielectric properties measured by dielectric resonator methods at 5-7 GHz. A potentially useful temperature-compensated dielectric ceramic was found at the composition $0.67Ca_2AlNbO_6$:$0.33Ca_3Nb_2O_8$.

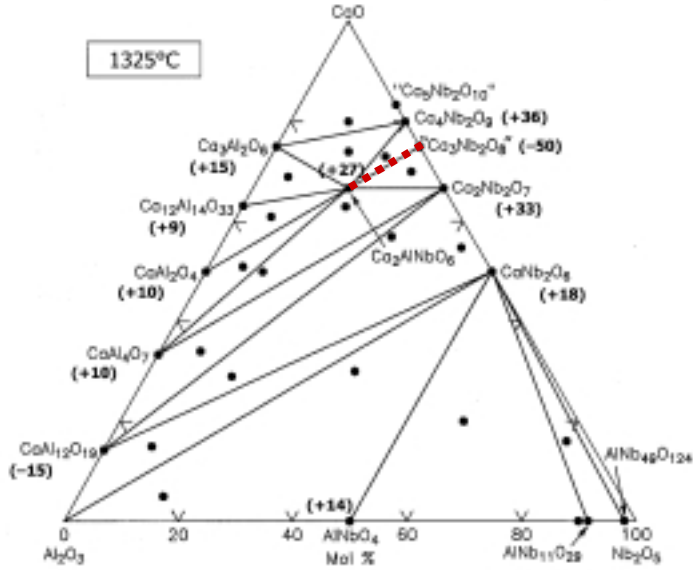

Subsolidus phase equilibria relations found in the CaO:Al_2O_3:Nb_2O_5 system in air. The dielectric constants and the signs of their temperature dependences are included for selected compounds. Ca_2AlNbO_6 and $Ca_3Nb_2O_8$ occur in equilibrium with each other and exhibit opposite signs of τ_ε. A stable, temperature-compensated ceramic was found at the composition $0.67Ca_2AlNbO_6$:$0.33Ca_3Nb_2O_8$.

Subsolidus phase equilibria in the SrO-Al_2O_3-Nb_2O_5 system were determined by synthesis of 75 compositions between 1200 °C and 1600 °C in air. As shown in the diagram below, three ternary compounds were observed, including the known double-perovskite, Sr_2AlNbO_6, and two new phases, Sr_4AlNbO_8 and $Sr_{5.7}Al_{0.7}Nb_{9.3}O_{30}$. Sr_4AlNbO_8 is unstable above 1525 °C and forms with a monoclinic unit cell elucidated by electron diffraction and refined using X-ray powder diffraction data; attempts to grow single crystals of this phase for complete structure determination were unsuccessful. $Sr_{5.7}Al_{0.7}Nb_{9.3}O_{30}$ ($Sr_{6-x}Al_{1-x}Nb_{9+x}O_{30}$, x=0.3) forms with the tetragonal tungsten bronze structure melts incongruently near 1425 °C, and occurs as essentially a point compound, with little or no range of x-values. Difficulties encountered preparing this compound as well as its limited composition region indicate that the tungsten bronze structure

has a narrow stability region in this chemical system, probably resulting from the relatively small size of Al^{3+}. The existence of an extensive cryolite-like solid solution, $Sr_3(Sr_{1+x}Nb_{2-x})O_{9-3/2x}$, occurring between $Sr_4Nb_2O_9$ (x=0) and $Sr_6Nb_2O_{11}$ (x=0.5), was confirmed, with cubic lattice parameters. Dielectric properties were measured for the three ternary compounds at frequencies between 3 GHz and 10 GHz.

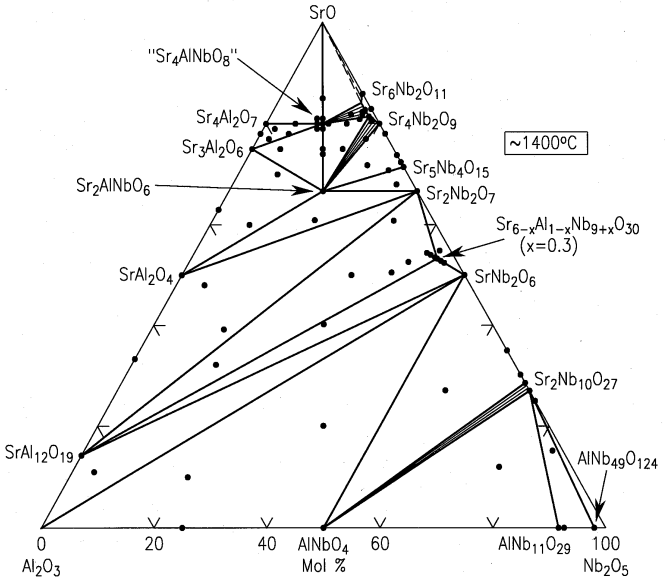

Subsolidus phase equilibria relations in the SrO-Al_2O_3-Nb_2O_5 system determined in air. Three ternary compounds were confirmed; "Sr_4AlNbO_8", Sr_2AlNbO_6, and $Sr_{5.7}Al_{0.7}Nb_{9.3}O_{30}$ ($Sr_{6-x}Al_{1-x}Nb_{9+x}O_{30}$, x=0.3). The first two compounds exhibit close-packed perovskite-related structures, while the last forms with a framework-type tetragonal tungsten bronze structure.

The subsolidus phase relations in the ternary system BaO-Al_2O_3-Nb_2O_5 have also been determined. The phase diagram has revealed the existence of a new ternary composition with the tetragonal tungsten bronze (TTB) structure occurring at the composition $Ba_{5.75}Al_{0.75}Nb_{9.25}O_{30}$ ($Ba_{6-x}Al_{1-x}Nb_{9+x}O_{30}$, x=0.25). As was found in the analogous SrO-system, this TTB-type phase melted incongruently (near 1300°C), and occurs as essentially a point compound, with little or no range of x-values. Variable-temperature capacitance measurements indicated that this compound is non-ferroelectric. Solid solutions with TTB-related structures occurring along the BaO-Nb_2O_5 binary were also found to extend into the ternary, dissolving several percent mol fraction Al_2O_3.

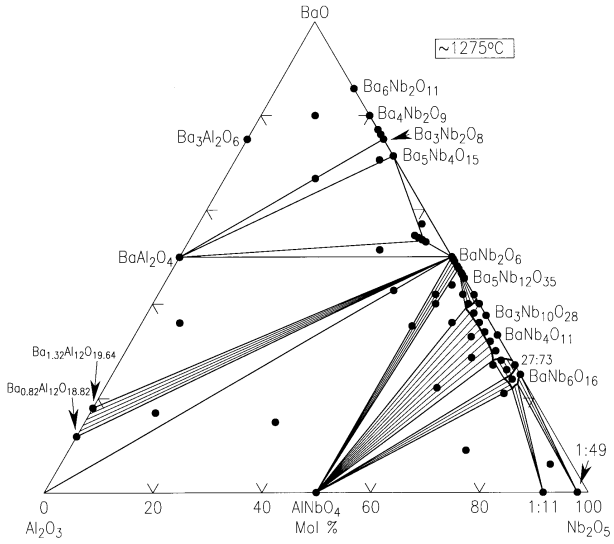

Subsolidus phase relations in the system BaO-Al_2O_3-Nb_2O_5. One ternary compound with the tetragonal tungsten bronze structure was found to occur, along with two single-phase regions with TTB-like structures extending in from the BaO-Nb_2O_5 binary system.

Rolando and Grassi reported phase equilibria in the MgO-Al_2O_3-Nb_2O_5 system in 1976. The study, conducted at 1400°C, revealed no ternary compound formation, as shown in the diagram here. Considerable solid solution formations were reported; however, the extensive solid solution formation shown here for the phase $AlNbO_4$ was not observed in our studies of the CaO-, SrO-, and BaO- systems.

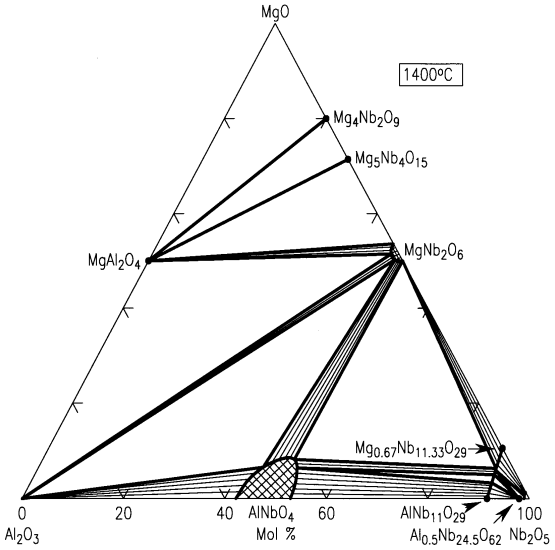

Phase equilibria in the MgO-Al_2O_3-Nb_2O_5 (Rolando & Grassi, 1976) showing the formation of no ternary compounds, in contrast to the other systems

For More Information On This Topic

T.A. Vanderah, W. Febo, Julia Y. Chan, R.S. Roth, J.M. Loezos, L.D. Rotter, R.G. Geyer, and D.B. Minor, "Phase Equilibria and Dielectric Behavior in the CaO-Al_2O_3-Nb_2O_5 System", *J. Solid State Chem.* **154**, xxx (2000).

Julia Y. Chan, I. Levin, T.A. Vanderah, R.G. Geyer, and R.S. Roth, "Subsolidus Phase Relations and Dielectric Properties in the SrO-Al_2O_3-Nb_2O_5 System", *Int'l. J. Inorg. Mats.* **2**(1), 107-114 (2000).

Contact: T.A. Vanderah, I. Levin

First-Principles Calculation of Dielectric Permittivity in Microwave Materials

One of the criteria of dielectric materials for microwave applications is that they have high permittivity (dielectric constant). In this project, we demonstrated that density-functional theory methods, using only the crystallographic cell parameters and space group as experimental input, can be used to compute dielectric permittivities, and that good agreement with experiment is obtained. In particular, we focused on $CaTiO_3$ and $CaAl_{1/2}Nb_{1/2}O_3$. These two materials have nearly the same structure, yet the permittivity of $CaTiO_3$ is nearly 10 times larger than that of $CaAl_{1/2}Nb_{1/2}O_3$. Our calculations reproduce the different dielectric behaviors. Furthermore, they show that the differences in permittivity are due in large part to the different phonon properties of the lowest-frequency phonons in the two systems and suggest that these differences in turn are related to differences in electronic structure.

Dielectric materials for microwave applications must have high permittivity, low loss, and temperature stability. Uncovering the relationship between chemistry, structure, and dielectric properties is of the utmost importance for the rational design of new dielectric materials. The contrasting dielectric properties of the closely related materials $CaTiO_3$ (CT) and $CaAl_{1/2}Nb_{1/2}O_3$ (CAN) highlight the need for fundamental studies of structure-property relationships. CT is a simple perovskite; CAN is a doubled perovskite with a rocksalt-like 1:1 ordering of Al and Nb on the B-site sublattice. CT and CAN have nearly identical lattice parameters, tolerance factors, and octahedral tilting patterns and magnitudes (Figure 1).

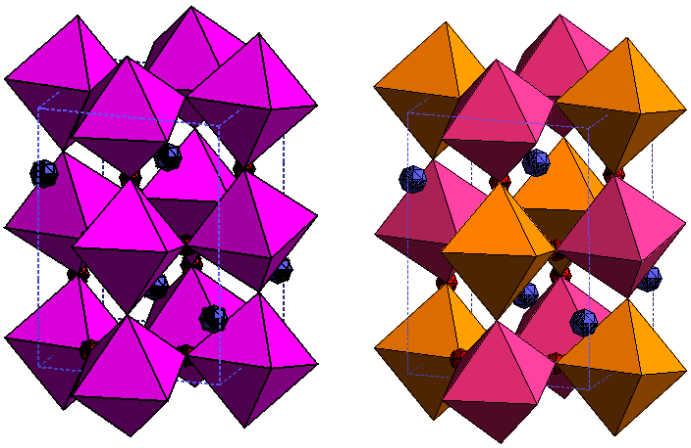

Figure 1

Experimentally, however, CT has dielectric permittivity $\kappa \sim 170$ and and a temperature coefficient of resonance frequency $\tau_f \sim +900$ at room temperature whereas CAN has $\kappa \sim 27$ and $\tau_f \sim -88$ MK^{-1}. Furthermore, the CT-CAN system is of experimental interest because it forms a solid solution series across the entire composition range and thus contains a single-phase material with $\tau_f = 0$, which is potentially a useful microwave dielectric material.

All calculations are performed using VASP (the Vienna ab initio simulation package). VASP is a code for plane-wave pseudopotential density functional theory calculations. The highest-precision options were used for well-converged results. We used the experimental lattice parameters and space group as the only input. The ionic positions in each system were relaxed to equilibrium. Then, by perturbing each ionic positions in the relaxed structure in turn and calculating the change in interatomic forces and polarization, we obtained the phonon properties of each system.

In order to understand the structure-property relationships that lead the simple perovskite CT to have a higher permittivity than the the double perovskite CAN, we turned to first-principles calculations. All calculations are performed using VASP (the Vienna ab initio simulation package) which is a code for plane-wave pseudopotential density functional theory calculations. We used the experimental lattice parameters and space group as the only input. The ionic positions in each system were relaxed to equilibrium. Then, by perturbing each ionic positions in the relaxed structure in turn and calculating the change in interatomic forces and polarization, we obtained the phonon properties of each system.

Finally, dispersion theory is used to relate the dielectric constant of a system to its calculated phonon properties. The results are shown in Figure 2. The computed dielectric constant is 275.0 for CT and 25.3 for CAN. These compare very well with the experimental values. The reasons for the discrepancies are two-fold. First, whereas density-functional theory is exact in principle, the exact formula is unknown. Any result obtained is inexact. Second, the dispersion formula assumes a harmonic system. In real systems, interatomic forces are anharmonic which affects the dielectric properties.

Nonetheless, the agreement with experiment is good enough to allow us to understand the reasons for the different dielectric behaviors. As can be seen in Figure 2, the dielectric response of CT is dominated by that of its three lowest-frequency phonons near 100 cm^{-1}. The corresponding phonons in CAN occur at higher frequencies and with lower effective charges than in CT. Both trends suppress the dielectric constant, which mathematically depends on the ratio of the effective charge to frequency.

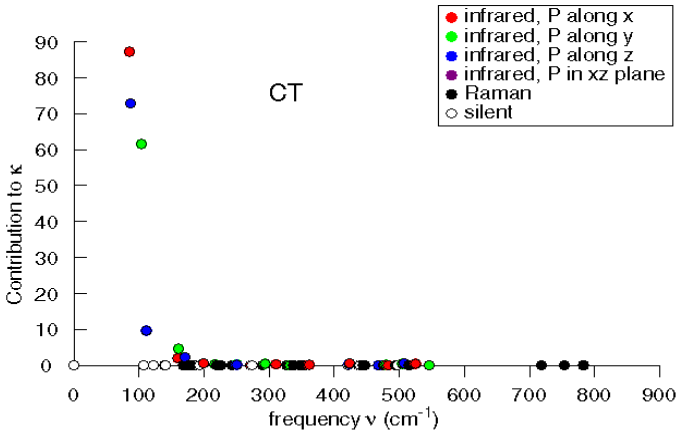

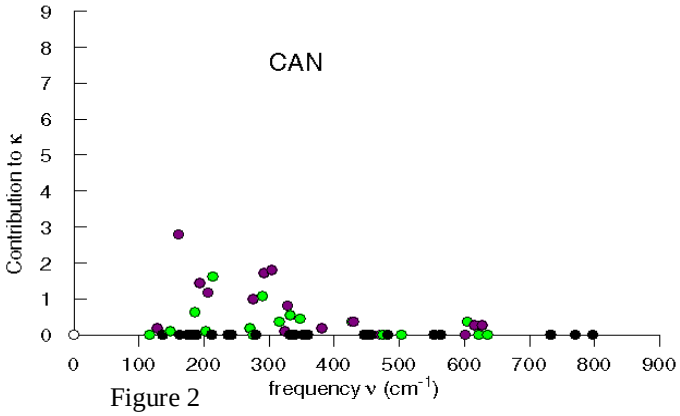

Figure 2

The differences in frequencies arise from all the interatomic forces and it is difficult to pinpoint the reasons for the differences. The different effective charges on the other hand, are clearly related to differences in the nature of the phonons eigenvectors (Figure 3). In CT, both Ca and Ti move against the oxygens in the lowest frequency polar phonons. The net polarization is maximized when positive and negative charges move in opposite directions. In CAN, on the other hand, Ca moves against the O, but Al and Nb both move with the oxygens, which suppresses the overall charge displacement.

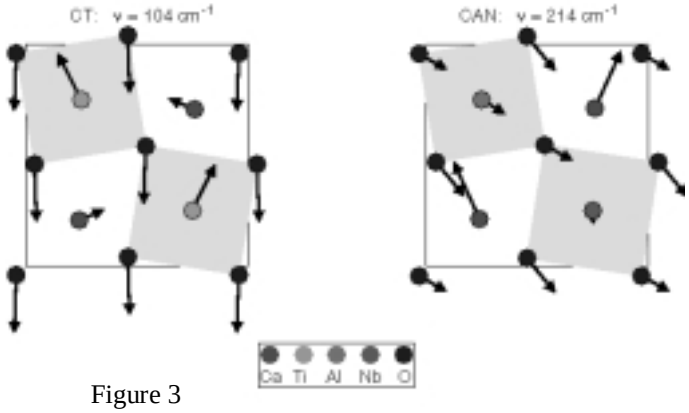

Figure 3

Why do B site cations (Ti,Al,Nb) move against the O in CT but not in CAN? We first note that in the case of simple perovskites involving Nb, such as $KNbO_3$ (KN), Nb moves against the oxygens in the lowest-frequency polar modes. This difference in the behavior of Nb in CAN and KN is not due to size effects: the Nb-O distances in the two compounds are almost identical. We look instead at differences in electronic structure.

It is well known that hybridization of oxygen 2p and B site transition metal d electrons is very important for the lattice dynamics of perovskites. One expects an inverse relationship between the importance of covalent bonding in a perovskite and the band gap, all other factors being the same. With this in mind, we calculated the band gaps in CT, CAN, and KN. Our results support the hypothesis that larger band gaps lead to reduced importance of covalent bonding and less tendency of B site cations to move against the oxygens in the low-frequency phonons. The reason for the larger gap in CAN than KN is due to the presence of the Al. The Al ions contribute no low-lying energy levels to the conduction bands. The lowest-lying conduction states come mainly from Nb-4d electrons. In a simple perovskite with Nb on every B site, the lowest conduction state wavefunction is spread over all the B sites and is more plane-wave-like than in a complex perovskite where Nb and thus the wavefunction is distributed on only half the sites. The more localized wavefunctions in the complex perovskite lead to higher eigenenergies and thus a larger band gap. It will be interesting to see how the type and ordering of the B site cations affect the electronic structure, phonon behavior, and dielectric properties of complex perovskites in general.

For More Information On This Topic

Cockayne, E., "Comparative Dielectric Response in $CaTiO_3$ and $CaAl_{1/2}Nb_{1/2}O_3$ from First Principles", submitted to J. Appl. Phys.

Contact person: Eric Cockayne.

New Methodologies to Characterize Machining Damage and Its Effect on Strength in Ceramics

Cost effective means to machine ceramics with a minimum of machining induced surface damage are of considerable importance. One component of the NIST Ceramics Division's Ceramic Machining Consortium and Mechanical Test Method Standardization programs has been a study to characterize and evaluate the effects of machining on ground surfaces of ceramic cylindrical rods and rectangular test bars. Test methods to evaluate machining damage and fractographic tools to detect machining cracks have been developed and refined.

Manufacturing processes for a variety of ceramic materials and applications require grinding for shaping and final finishing. When applied to load bearing ceramic components, a critical aspect of a grinding process is the extent to which grinding induced damage affects the strength and reliability of the component. Thus, measurements to determine the effects of grinding damage and the characterization of grinding damage are critical to the development of cost effective ceramic grinding processes. Three significant accomplishments for this year have been (1) development of simple fractographic means for identification of machining cracks, (2) finalization of the development of a test method for measuring the flexure strength of cylindrical rod specimens), and (3) completion of a comprehensive analysis on a particular sintered reaction-bonded silicon nitride. Much of the work leading to these accomplishments was conducted in association with projects undertaken by the NIST Ceramic Machining Consortium. An important goal of the Consortium has been the determination of the effect of different grinding conditions on the flexure strength of commercially significant ceramic materials. Realization of this goal has required the development of new test methods and better means for the identification machining damage.

Machining cracks can be difficult to detect on fracture surfaces even if a fracture mirror identifies the fracture origin area. Machining cracks that extend beneath the surface by 20 μm to 50 μm often blend into the background microstructure, especially in ceramics with elongated grain microstructures designed to enhance toughness. The microstructural irregularities create a rougher fracture surface and subtle machining cracks may be impossible or difficult to detect. In the past, the usual practice has been to grind then break some bend bars. If a strength loss relative to some baseline value was detected, it was inferred that machining cracks must have been present. Sometimes this analysis was supplemented by rudimentary fractographic examination to at least verify that the origins were located on the specimen surface. This approach was not infallible, however, since many inherent material flaws may reside by chance at or near the surface. It is unreasonable to arbitrarily characterize such origins as machining flaws.

A new simple fractographic means to detect transverse machining cracks with a minimum of fuss has been discovered. Some cracks have characteristic telltale features that can be detected with low power optical microscopy. In other cases, the fracture mirror itself has certain telltale, noncircular shapes and it could reliably be inferred that machining damage or a scratch was strength limiting without actually seeing the machining crack itself! The new practices are general and not material specific and they may be used by even novice fractographers. The telltale features have been detected in other ceramics, glasses, and even single crystals. These new fractographic methods will be incorporated into several ASTM standards.

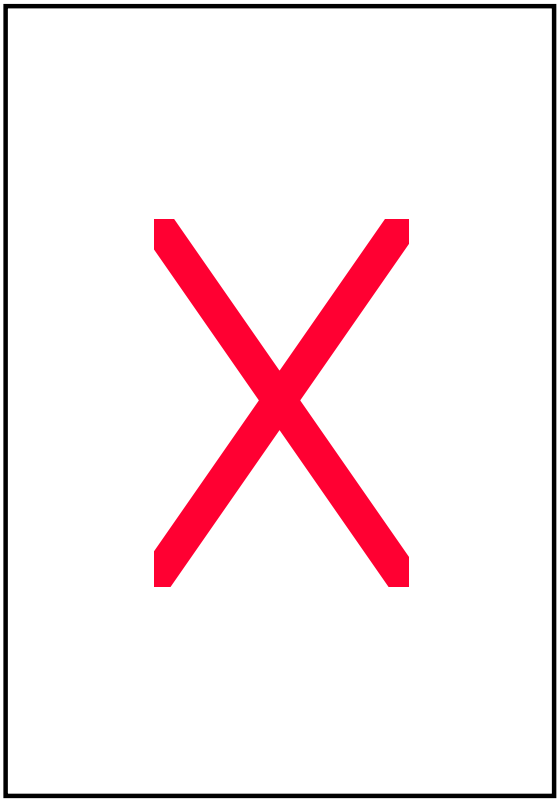

Figure 1 Fracture surface of a ground silicon nitride rod with a machining crack fracture origin.

Flexure testing may be used to investigation the effects of surface grinding processes on strength. In the past, strength measurements have predominantly been on rectangular bars using standard test methods. However, only planar grinding modes are used to machine rectangular bars, effectively limiting such investigations to those modes of grinding. In fact, the majority of ceramic parts are cylindrical or circular in cross section requiring cylindrical and centerless grinding modes for fabrication. In response to this clearly identified need, a project was undertaken to develop flexure test methods applicable to cylindrical rods. This effort has led to the design of a flexure test fixture (shown below) and verification of its performance.

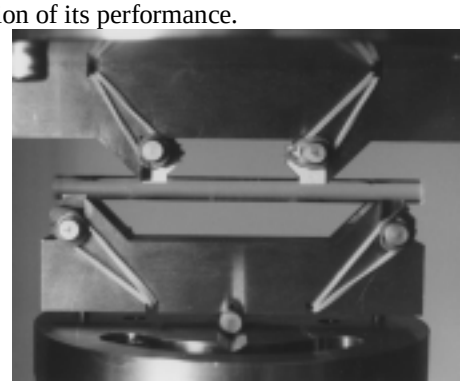

Figure 2 The new fixture for flexural strength testing with a glass rod specimen.

The cylindrical rod flexure test method was applied to a Consortium project designed to investigate the effect of finish grinding conditions on the flexure strength of a commercial sintered reaction-bonded silicon nitride that is in use in heavy-duty diesel engines. The engine component is cylindrical in shape and finish machining by centerless grinding is a key step in the manufacturing process.

Figure 3 shows the results of the study. The figure is a Weibull probability plot showing the distribution of flexure strengths of sets of rods and rectangular bars. The rods were centerless or cylindrically ground. Baseline strength data were obtained by grinding in the longitudinal direction with a 320 grit resin bond diamond wheel. Using the same wheel and grinding conditions, but grinding in the transverse direction, it is seen that flexure strength is substantially lower. When the same experiment was repeated with a finer 600 grit resin bond wheel, the flexure strengths in the longitudinal and transverse directions are nearly the same. Moreover, these strengths differ little from values obtained for the 320 grit wheel in the longitudinal direction. Accordingly, it might be hypothesized that, for these sets of specimens, fracture did not originate at grinding damage and probably initiated at intrinsic flaws in the material.

A detailed fractographic examination was conducted on all specimens and it confirmed that fracture originated at inclusions, pores, sintering irregularities, or other microstructural imperfections inherent to the material. In contrast, by utilizing the fractography methods described earlier it was found that fracture of the 320 grit transverse ground specimens was due to machining damage. A key finding from this work was that 600 grit transverse finish grinding created negligible or minor damage to this particular silicon nitride. Such machining is simpler and more cost effective than longitudinal grinding in manufacturing cylindrical parts.

The new flexure test methodology for cylindrical rods has been refined to the point that testing is routine and just as easy as testing the more traditional rectangular bend bars. It is anticipated that this will open the way to flexural strength investigations with the associated centerless and cylindrical modes of grinding. A new ASTM standard for cylindrical rod flexure testing will be the focus of work in FY 2001.

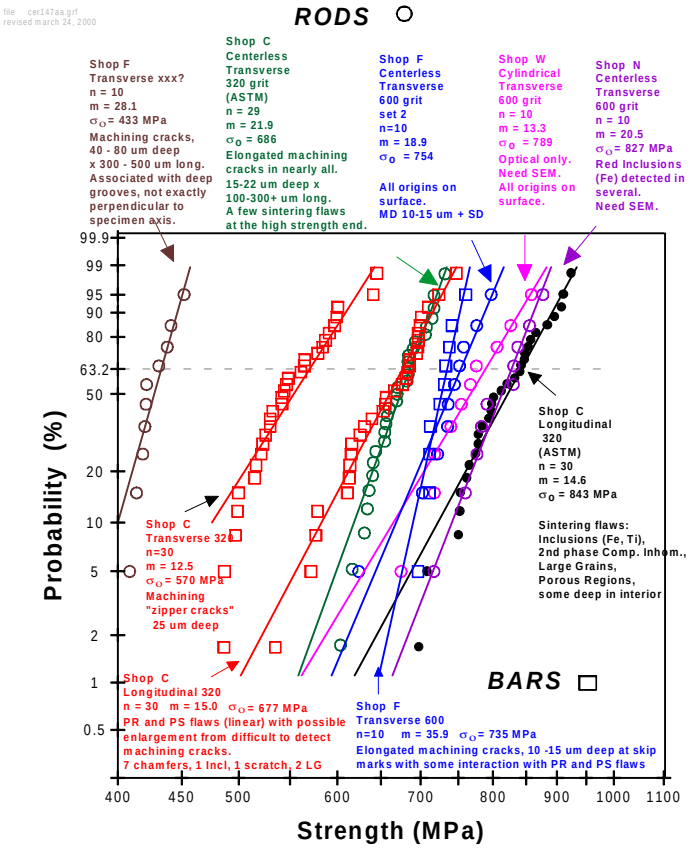

Figure 3 Weibull distribution graph of flexural strengths for a commercial silicon nitride.

For More Information On This Topic

Publications: G. D. Quinn, L. K. Ives, S. Jahanmir, and P. Koshy, "Fractographic Analysis of Machining Cracks in Silicon Nitride Rods and Bars," presented at the 4th International Conference on the Fractography of Glasses and Ceramics, Alfred University, July 2000, to be publ., Ceramic Transactions, eds, J. Varner, G. Quinn, V. Frechette, American Ceramic Society, Westerville, OH, 2001.

Contacts: George Quinn. And Lewis Ives

NIST Recommended Practice Guide

In 2000, we produced the first NIST Recommended Practice Guide, SP 960-1, " Particle Size Characterization" by Ajit Jillavenkatesa, Stanley Dapkunas, and Lin-Sien Lum. The Guide synthesizes information on the measurement of ceramic particle size, providing a broad perspective of methods of size measurement, sampling, data analysis, and identification of relevant standards

The Recommended Practice Guide series is a new approach for delivering information to the ceramics community and provides an easily accessed and understandable source of practical knowledge. The Practice Guide series synthesizes the wealth of experience and data developed at NIST over many years on specific topics. This information is generally published in the scientific literature over several years and may not be readily available. The Guide series is intended for scientists and engineers who are not familiar with particular measurement technologies and who require a general perspective.

Determination of particle size distribution is a critical step in almost all ceramic processing techniques. However, particle size analysis techniques are often applied and/or results interpreted inappropriately, primarily due to a lack of understanding of the underlying principles of size analysis, or due to confusion arising from claims and counter-claims of the analytical ability of size determination techniques and instruments. "Particle Size Characterization" has been written to address some of these issues and concerns. The Guide is not an exhaustive and comprehensive text on particle size analysis, but attempts to convey the practical issues that need to be considered when conducting analysis by some of the techniques commonly used in the ceramics community. Data and information from studies conducted over years of participation in international round robin tests and standards development have been used in developing the information in the Guide. The Guide also provides comparative data on different measurement methods applied to the same material, as illustrated in Figure 1.

"Particle Size Characterization" explains the physical principals involved for most broadly used methods of measurement or characterization, provides general procedures for each method, identifies sources of error and variation, describes methods of data analysis , and lists relevant national and international standards. The Guide was reviewed by individuals in industry to ensure that it provides information that is both useful and usable by those concerned with particle size characterization.

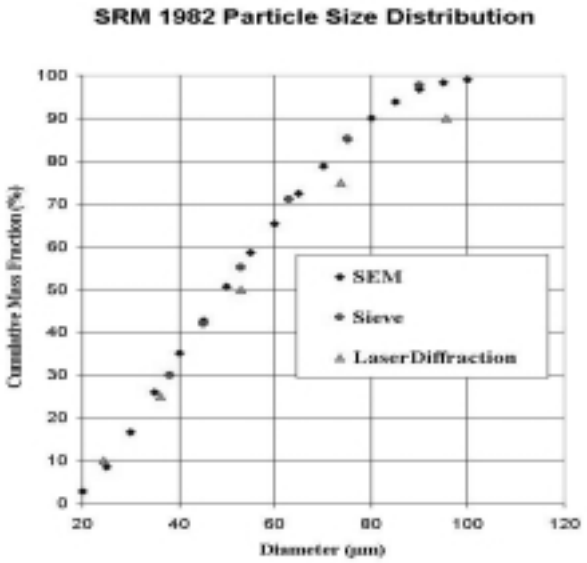

Figure 1. Comparison of Particle Size Distribution for NIST SRM 1982 Measured by Three Techniques

Specific topics covered in " Particle Size Characterization" include:

- powder sampling,
- sieving techniques,
- x-ray gravitational sedimentation techniques,
- microscopy based techniques,
- laser light diffraction techniques,
- reporting size data; and
- a glossary of terms.

The NIST Recommended Practice Guide for Particle Size Characterization, Figure 2,will be followed by two other Guides for the ceramics community: Nomenclature for Particle Dispersion Technology and Rheological Measurements; and, Design with Brittle Materials.

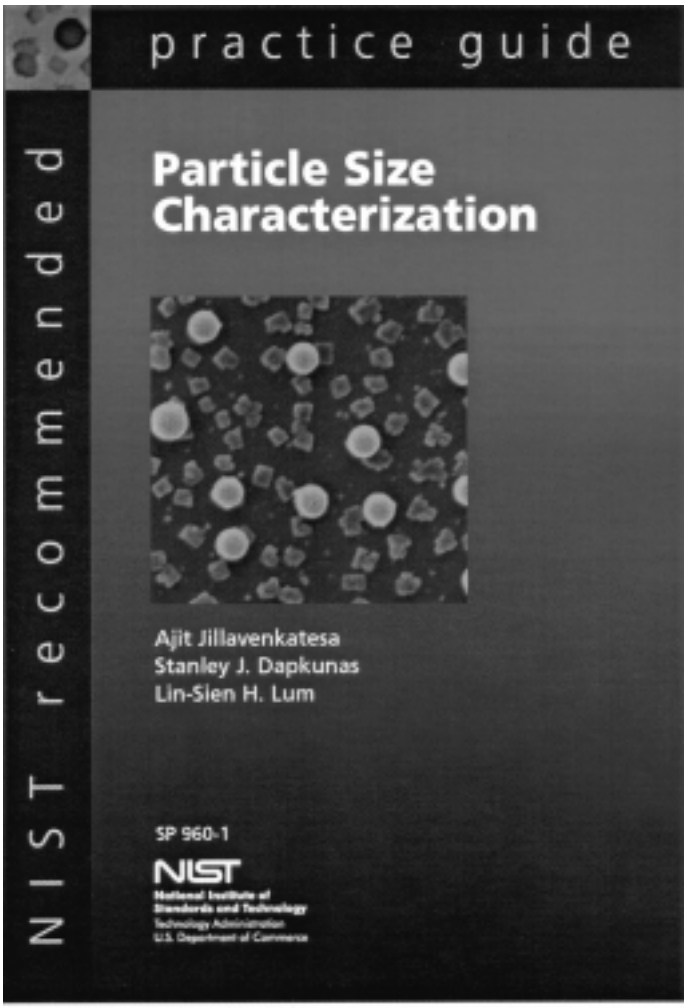

Figure 2. NIST Recommended Practice Guide, SP 960-1, “Particle Size Characterization” (picture of the cover)

The NIST Recommended Practice Guide for Particle Size Characterization may be obtained from the Ceramics Division office at 301/975-6119 or carolyn.sladic@nist.gov. The Guide will also be available at the Ceramics Division Website, www.ceramics.nist.gov.

For More Information

On This Topic

Ajit Jillavenkatesa and S. J. Dapkunas, Ceramics Division

Phase Equilibria of Ba-Nd-Cu-O, and Critical Single-Phase Region for Tailoring Superconducting Properties of $Ba_{2-x}(Nd_{1+x-y}Yb_y)Cu_3O_{6+z}$

By mixing of the smaller Yb ion with Nd in $Ba_{2-x}Nd_{1+x}Cu_3O_{6+z}$ (Nd-213) superconductor, both flux-pinning and melting properties can be tailored and optimized. To provide the basis for this effort, we have determined the phase diagram of the BaO-Nd_2O_3-CuO_x system, as well as the single phase region of $Ba_{2-x}(Nd_{1+x-y}Yb_y)Cu_3O_{6+z}$ under atmospherically controlled conditions. The diagrams of BaO-Nd_2O_3-CuO_x determined under purified air and 0.1% O_2 are similar, but substantially different from the literature data, which were determined using $BaCO_3$. The extent of the solid solution decreases, while the onset temperature of the T_c values increase as the oxygen partial pressure decreases. The locations of the single-phase boundaries provide information important for processing flux-pinned materials, and will facilitate rapid advancement of the second generation RABiTS/IBAD coated conductor technology.

The relatively recent success in preparing $BaR_2Cu_3O_{6+z}$ materials with promising superconducting properties via the RABiTS and IBAD processes has revitalized research interest in BaO-R_2O_3-CuO_x systems. In particular, the BaO-Nd_2O_3-CuO_x system is one of the most promising lanthanide systems for the development of high T_c superconductors. $BaNd_2Cu_3O_{6+Z}$ (Nd-213) demonstrates a high T_c value as well as high vortex-pinning by comparison with $Ba_2YCu_3O_{6+x}$. Because of the formation of a large region of solid solution in $Ba_{2-x}Nd_{1+x}Cu_3O_z$ associated with the substitution of Nd on the Ba site, one can control physical properties by varying the solid solution composition. Furthermore, by substituting Nd with the smaller Yb ion, one can tailor both superconducting and melting properties of $Ba_{2-x}(Nd_{1+x-y}Yb_y)Cu_3O_{6+z}$.

An experimental procedure has been successfully established to study phase diagrams under controlled atmosphere while minimizing the presence of CO_2, which results in the formation of carbonates, especially in the presence of BaO, and incorrect phase equilibria data. .

The diagrams of BaO-Nd_2O_3-CuO_x determined under purified air and 0.1% O_2 (Fig. 1) are very similar, but substantially different from the literature data, which were determined using $BaCO_3$. The BaO-Nd_2O_3-CuO_x system consists of three solid solutions and one stoichiometric compound. The first solid solution is the high T_c series, $Ba_{2-x}Nd_{1+x}Cu_3O_z$. We have confirmed that the extent of this solid solution is greater than previously reported, and that it extends from x = 0 to 0.95. Two phase transformations occur within this solid solution instead of the commonly known single transformation. These transformations progress from orthorhombic tetragonal and then to orthorhombic (Fig. 2), according to electron microscopy studies. The second series, $Ba_{1+x}Nd_{2-x}CuO_z$, (the 'brown-phase') has only a narrow solid solution region when prepared in air or in 0.1% O_2. $Ba_2Nd_4Cu_2O_z$ was found to be antiferromagnetic, but showed ferromagnetic behavior as Nd was partially substituted by La The $Ba_2(Nd,La)_4Cu_2O_z$ phase may provide desirable magnetic pinning centers for processed Nd-213 ceramics. In the high Ba-content region, the orthorhombic solid solution

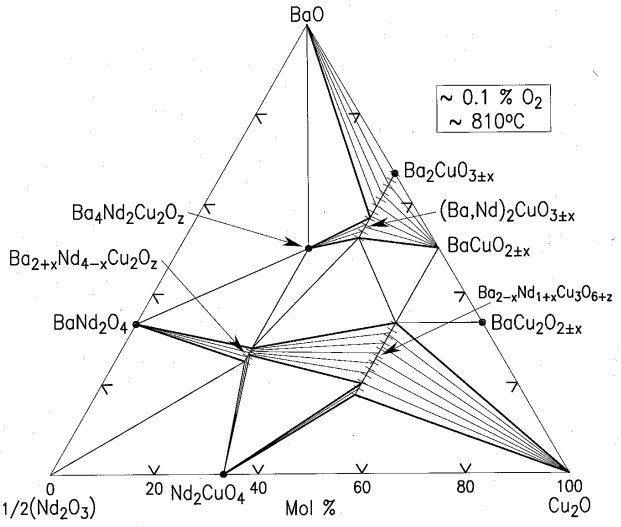

Fig. 1. Phase diagram of the BaO-Nd_2O_3-CuO_x system

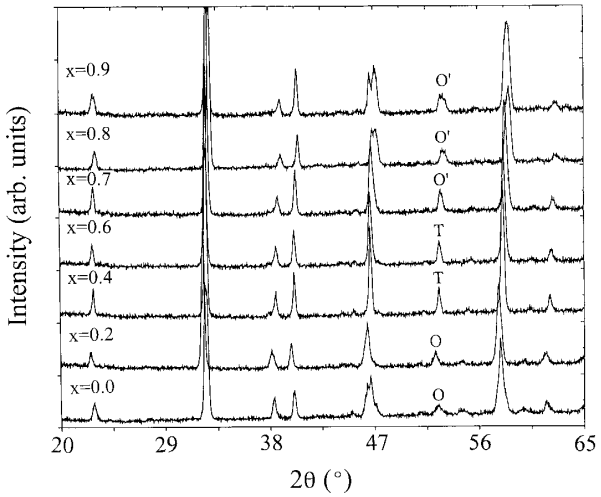

Fig. 2. X-ray patterns of $Ba_{2-x}Nd_{1+x}Cu_3O_z$ in 0.1% O_2

$(Ba_{2-x}Nd_x)CuO_{3-z}$ and a nominally stoichiometric phase, $Ba_4Nd_2Cu_2O_z$, were confirmed. The latter is an insulator which consists of unusual 1-dimensional corner-sharing CuO_5 linear chains. In the boundary BaO-CuO_x system, two phases were found when the system was prepared in air, namely, Ba_2CuO_3 and CuO; an additional $BaCu_2O_2$ phase was found in the diagram prepared under 0.1% O_2. Only Nd_2CuO_4 and $BaNd_2O_4$ were found in the Nd_2O_3-CuO_x and BaO-Nd_2O_3 systems, respectively. The structure of $BaNd_2O_4$ was studied by neutron diffraction using the Rietveld method.

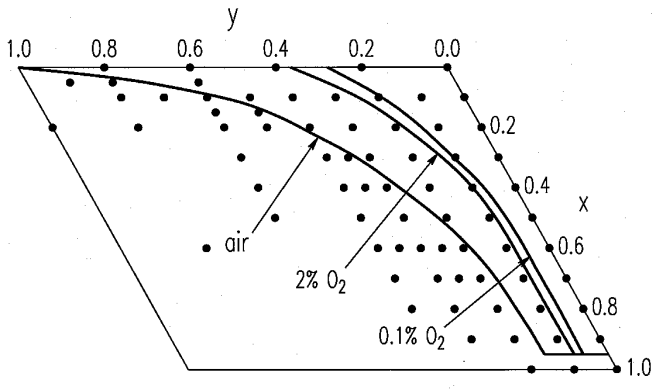

Fig. 3. Single phase regions of $Ba_{2-x}(Nd_{1+x-y}Yb_y)Cu_3O_{6+z}$

The range of the single-phase solid solution region for the phase $Ba_{2-x}(Nd_{1+x-y}Yb_y)Cu_3O_{6+z}$ has been determined as a function of oxygen partial pressure. Figure 3 shows a composite diagram of the single phase region (to the right of the curves) under 0.1% O_2 (810 ºC), 2% O_2 (810 ºC) and air (930 ºC). In Fig. 3, parallel to the x compositional axis, the samples have constant Yb content, while the Ba concentration changes as a result of substitution by Nd. Parallel to the y compositional axis, Yb and Nd substitute for each other while the Ba is kept constant. The extent of the single-phase region decreases as the oxygen partial pressure decreases.

As Nd substitutes for Ba, a sequence of phase transformations similar to that for the Nd-213 solid solution was determined. Neutron Rietveld refinements on selected compositions indicated that Yb substituted exclusively for Nd and not Ba, while Nd substituted for Ba. As Nd substituted on the Ba sites, the oxygen content of the samples increased, and oxygen and copper site disorder was also observed.

The onset melting temperatures decreased as Yb substituted for Nd, and also as Nd substituted for Ba. For example, the initial melting temperatures of the $Ba_{2-x}(Nd_{1+x-y}Yb_y)Cu_3O_{6+z}$ series with y = 0.1 decreased from 1080 ºC for x = 0.1 to 1058 ºC for x = 0.7. The onset T_c value decreased as the annealing oxygen partial pressure increased, and as the amount of Nd increased. Substitution of Nd^{3+} on Ba^{2+} is thought to cause progressive reduction of the hole concentration on the CuO plane.

The structural, melting and superconductivity data discussed above are critical for processing and for tailoring flux-pinned materials. Future research on Ba-R-Cu-O phase equilibria will focus on the R =Y , Sm systems, and on the Nd/Y mixed lanthanide system under reduced oxygen pressures.

For More Information On This Topic

1. Wong-Ng, W., Cook, L.P.,. Suh,J., Coutts,R., Levin, I., Stalick, J. "Phase Equilibria Diagrams of the BaO-Nd_2O_3-CuO_x system in Purified Air and 0.1% O_2" to be submitted to J. Solid State Chem.
2. Wong-Ng, W., Swartzendruber, L., Kaduk, J.A., Bennett, L.H., "Magnetic and Structural Properties of the 'Brown Phase' Solid Solution $Ba(Nd_{2-x}La_x)CuO_5$", submitted to J. Mag. and Mag. Mater.

Contact persons: Winnie Wong-Ng and Lawrence Cook

Polymer Chain Relaxation: Surface Outpaces Bulk

The time scale that controls polymer chain relaxation has taken on a new importance as the paradigm for polymer innovation evolves from three dimensions to two. Nanotechnology initiatives, involving the design and fabrication of highly confined polymer layers, drive the need for a comprehensive description of chain dynamics, as bulk polymers become thinner and more surface like. In this study we apply near-edge X-ray absorption fine structure (NEXAFS) to measure directly both surface and bulk segmental relaxation throughout a uniformly deformed polystyrene slab. Using this methodology, in a single experiment, chain relaxation is found to occur almost 50 % faster at the surface than in the bulk.

Rectangular samples (12.5 mm x 12.5 mm x 6 mm), prepared by

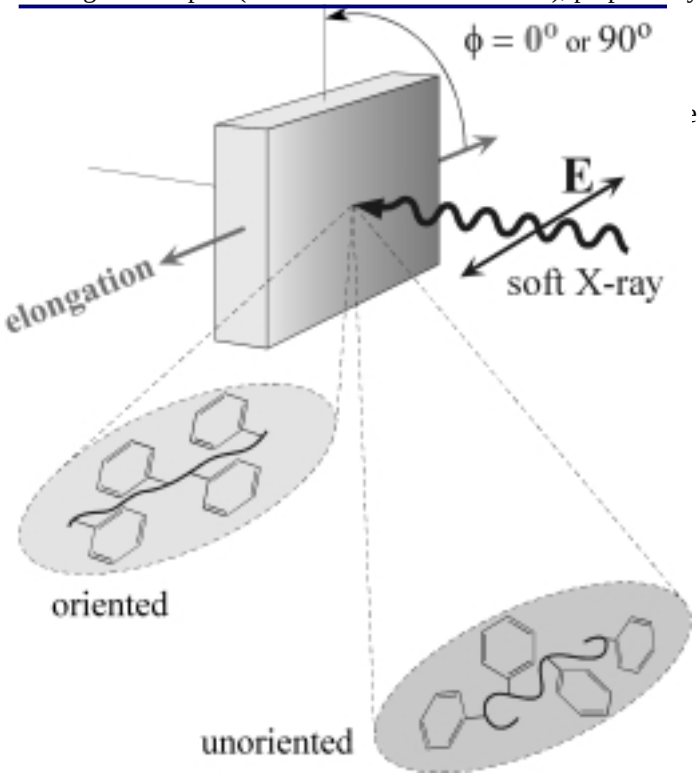

For each sample, PEY and FY were measured with the incident polarized X-ray beam normal to the sample surface and at two azimuthal sample orientations: with the electric field vector, **E**, parallel ($\phi = 0°$) and perpendicular ($\phi = 90°$) to the elongation direction as shown in the figure to the left.

Orientation of the chain backbone was determined by monitoring the C=C phenyl ring NEXAFS resonance intensity at 285.5 eV, which involves the excitation of carbon 1s electrons to the unfilled C=C antibonding orbitals of the phenyl ring. Enhancement of the C=C resonance intensity was observed when **E** was parallel to the elongation direction.

Since the phenyl C=C orbitals are oriented normal to the phenyl rings, and the phenyl rings, free to rotate around the pendant bond, will have a component normal to the chain axis, the intensity of the C=C signal has been shown to be an unambiguous signature of backbone orientation. This orientation, seen both in the PEY and the FY NEXAFS signals of the elongated samples, provides clear evidence of chain orientation at the outset of the experiment. A direct measure of the chain relaxation rates at the surface and in the bulk can be obtained by defining an orientation factor, OF (see fig. caption next page) that is evaluated from the time dependence of the C=C resonance intensity in the PEY (relative uncertainty ± 0.01%) and FY (relative uncertainty ± 0.05%) NEXAFS spectra, respectively, during annealing.

The schematic to the left details the sample geometry for the incident polarized soft X-ray beam normal to the polystyrene sample surface with the elongation direction parallel to **E** ($\phi = 0°$). The insets in the lower right represent chain configurations in oriented (before annealing) and unoriented (after annealing) elongated samples.

The graph shows that while the OF for both surface and bulk chains decays as a function of increasing annealing time at 60 °C, the surface orientation is initially greater and decays faster than for the bulk. Fitting the decay rates to exponential functions gives characteristic time constants of approximately 33 min and 50 min (with corresponding R^2 values of 0.90 and 0.91) for the surface and the bulk, respectively.

These results show conclusively that polystyrene surface chain relaxation dynamics are significantly faster than the bulk. Our results are in accord with recent theory predicting that collective motion on chain loops extended to the sample surface is responsible for a rapid increase of chain mobility near the surface region of the film (top ≈ 5 nm). The finding that the polystyrene surface segmental mobility greatly outpaces the bulk is expected to be a universal property of polymeric chains profoundly influencing the design, processing, and application of polymeric materials.

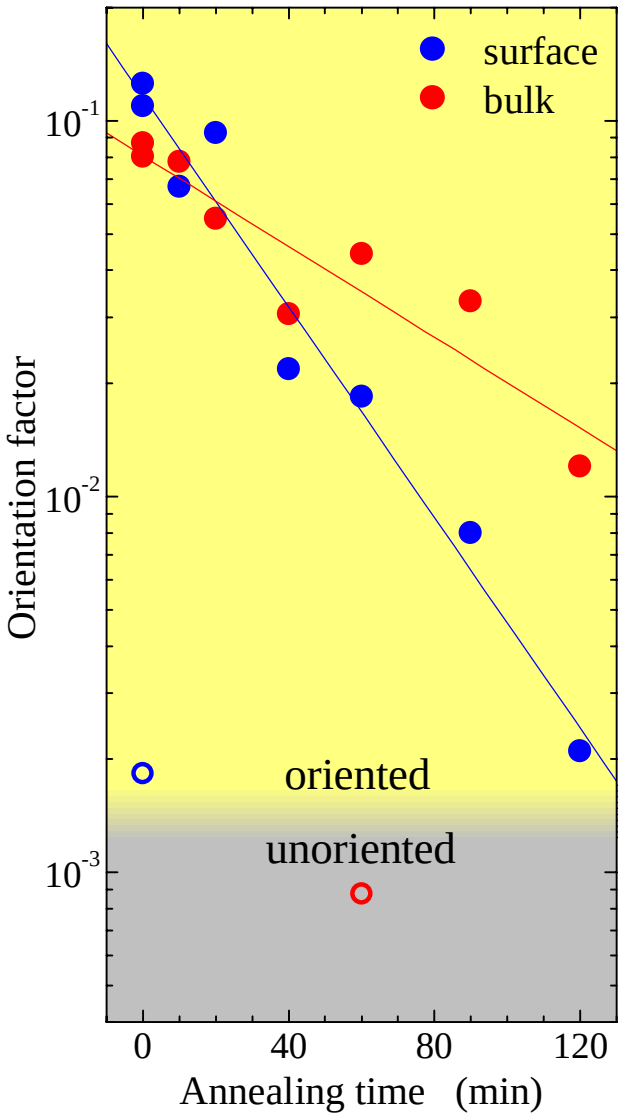

Figure right: Tme evolution of the orientation factor, OF, from an elongated (oriented) polystyrene sample reveals that when annealed at 60 °C the surface chains relax to an equilibrium (unoriented) configuration faster than the bulk chains. OF is calculated from $(I_{\parallel} - I_{\perp})/(I_{\parallel} + I_{\perp})$, where $I_{\parallel}$ and $I_{\perp}$ are the C=C resonance NEXAFS intensities collected with the sample elongation direction parallel ($\phi = 0°$) and perpendicular ($\phi = 90°$) to the electric vector of the soft X-ray beam, **E**, respectively. The blue circles denote OF from the partial electron yield NEXAFS signal (surface region) and the red circles represent the fluorescence yield NEXAFS signal (bulk region), measured simultaneously. The closed and open circles depict OF evaluated from data collected on elongated specimens and those not subjected to elongation, respectively. The solid lines represent exponential decay fits to the experimental data on the elongated samples; the rate decay constants are reported in the text.

For More Information

D. A. Fischer
W. E. Wallace, W. L. Wu (Polymers Divison)

On This Topic

K. Efimenko, J. Genzer (NCSU)

Spatially Resolved Valence Electronic Structure by X-ray Standing Waves and Photoelectron Spectroscopy

We have developed a new experimental method by which site specific valence electronic structure may be obtained. It utilizes the spatial variation of the electric-field intensity that occurs near a crystal x-ray Bragg reflection in conjunction with high-resolution valence-photoelectron spectroscopy to determine the partial densities of occupied valence states of crystalline materials. Resolution of the anion and cation contributions to the GaAs valence band is demonstrated and compared to an ab initio theoretical calculation of the Ga and As partial density of states.

One of the most powerful experimental tools for examining the electronic structure of a solid or film is photoelectron spectroscopy. Due to the conservation of energy between the incident photon and the ejected photoelectron, direct and important electronic information pertaining to the occupied valence-band density of states has been obtained for many materials. This information has been used to establish the validity of complicated band-structure calculations for metals, semiconductors, insulators, and alloys.

Typical photoemission measurements are performed with excitation sources that are monochromatic plane waves. As the intensity of a plane wave is constant over the dimensions of the crystalline-unit cell, standard photoemission measurements are unable to produce *direct*, site-specific valence information. However, such information is important for advancing our understanding of how chemical bonding results in the solid-state electronic structure.

Here we describe a new experimental method for obtaining site-specific valence-electronic structure. It utilizes the spatial variation of the electric-field intensity that occurs within the vicinity of a crystal x-ray Bragg reflection which is given by the superposition of the incident $\mathbf{E}_o$ and reflected $\mathbf{E}_h$ x-ray beams that travel with wave vectors $\mathbf{k}_o$ and $\mathbf{k}_h$, polarization vectors $\mathbf{e}_o$ and $\mathbf{e}_h$, and frequency ω:

$$\mathbf{E}(\mathbf{r},t) = [\ \mathbf{e}_o E_o e^{i\mathbf{k}_o\mathbf{r}} + \mathbf{e}_h E_h e^{i\mathbf{k}_h\mathbf{r}}\ ]\ e^{-i\omega t}.$$

$\mathbf{k}_o$ and $\mathbf{k}_h$ are connected by the Bragg condition $\mathbf{h} = \mathbf{k}_o - \mathbf{k}_h$, where $\mathbf{h}$ is a reciprocal-lattice vector of the crystal. For the σ-polarization geometry of a symmetric reflection, this field squares to give the electric-field intensity at an arbitrary point $\mathbf{r}$ in space:

$$I(\mathbf{r}) = |E_o|^2\ [\ 1 + R + 2\bullet\ R\cos(\ \nu + \mathbf{h}\cdot\mathbf{r}\ )\ ].$$

ν is the phase of the complex-field amplitude ratio $E_h/E_o = \bullet\ Re^{i\nu}$, and R is the reflectivity function $R = |E_h/E_o|^2$. Germane to the method is the unique ability to position the maxima (or minima) of the electric-field intensity at any location within the crystalline-unit cell by experimentally varying the phase of the complex reflectivity function between $0 < \nu < \pi$. This is achieved by slightly varying either the sample angle or the photon energy within the natural width of the crystal x-ray Bragg reflection.

Because the probability of emission of an electron from an atom in an external electric field is proportional to the electric-field intensity at the location of its atomic core (dipole approximation), by selectively positioning the electric-field intensity within the crystalline-unit cell and recording high-resolution valence-photoelectron spectra, spatially resolved components to the photoemission valence-band density of states may be directly obtained.

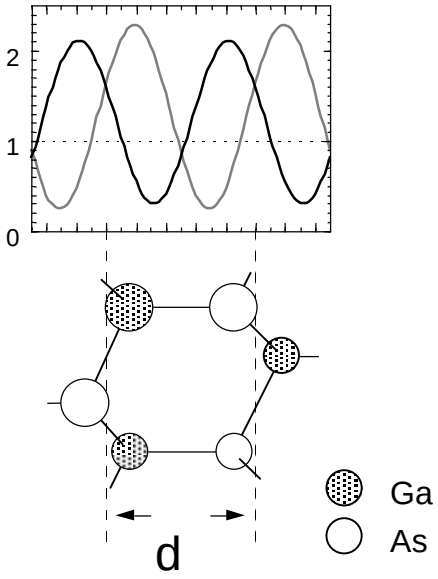

Figure 1: Theoretical calculation of the electric-field intensities and their spatial dependencies for different ν.

To illustrate the principal of the technique, Figure 1 shows a theoretical calculation of the electric-field intensities and their spatial dependence relative to the GaAs atomic planes for different values of ν within the photon-energy range of the GaAs(111) Bragg back-reflection condition. Significant contrast between the Ga and As contributions to both the core and valence photoelectron-emission spectra can therefore be obtained for this heteropolar zinc-blende crystal by simply experimentally varying the phase ν as demonstrated by Figure 2. The data in Figure 2 exhibit the well known x-ray standing wave effect for both the Ga 3d and As 3d core levels, as well as for the crystal valence band. Note either the enhancement or suppression of the relevant emission depending on which of the atomic planes (either Ga or As) was preferentially excited.

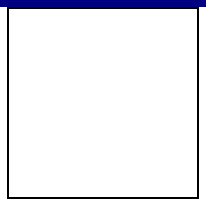

Figure 2: Photoemission spectra recorded from crystalline GaAs under the different electric-field conditions of Fig. 1.

In order to uniquely resolve the individual contributions to the GaAs valence band, we proceed as follows. Under condition of constant electric-field intensity, the valence photocurrent can be approximated as the linear sum of the individual partial-density of states $\rho_i(E)$ arising from the different i atoms of the unit cell weighted by the energy dependent, relative photoionization cross sections $\sigma_i(E,h\omega)$ of each of the states:

$$I(E,h\omega) \alpha \Sigma_i \rho_i(E)\sigma_i(E,h\omega).$$

For the case of a spatially dependent x-ray interference field, this expression must be modified to include the electric-field intensities at each of the different core sites:

$$I(E,h\omega) \alpha \Sigma_i \rho_i(E)\sigma_i(E,h\omega)[\ 1 + R + 2\bullet\ R\cos(\ \nu + \mathbf{h}\cdot\mathbf{r}_i\ )\ ].$$

Consequently, for a two atom unit cell such as GaAs, all that is necessary to uniquely resolve the individual chemical components of the GaAs valence band is to obtain valence spectra at two different electric field conditions and then solve a simple set of two linear equations.

Figure 3 shows the resulting chemically resolved components of the GaAs valence band obtained by taking the appropriate linear combinations of the spectra from figure 2. These components are compared to an *ab initio* theoretical calculation of the Ga and As partial-density of states computed by Professor James Chelikowsky's group at the University of Minnesota by using ab initio pseudopotentials within density functional theory with a plane-wave basis. The site-specific density of states curves were computed by using a sphere corresponding to the Ga-As covalent radius centered on each atom to deconvolve the obtained wavefunctions over atomic orbitals of valence electrons.

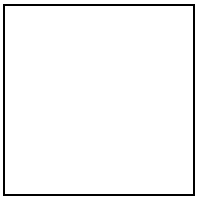

Figure 3: Comparison of the Ga and As partial density of states curves from both theory and experiment.

The calculations clearly show the differences between the two electronic structures centered around each atomic core. These differences occur due to the natural ordering of the Ga and As atomic 4s and 4p valence states, coupled with the solid-state bonding that has occurred between them and may be directly correlated with the crystalline band structure. Remarkable qualitative agreement between theory and experiment is observed, even though experimental resolution and cross-section effects have not been considered theoretically.

In conclusion, we have demonstrated that valence-photoelectron spectra recorded in the vicinity of a crystal x-ray Bragg reflection can reveal site-specific valence information that is directly related to the partial density of occupied valence states. It is our hope that this method will provide useful information pertaining to the detailed electronic structure of more complex crystalline materials that are currently of interest to the scientific community.

For More Information On This Topic

J.C. Woicik, E.J. Nelson, T. Kendelewicz, P. Pianetta, M. Jain, L. Kronik, and J.R. Chelikowsky, in press, Phys. Rev. B, *Rapid Communications*. J.C. Woicik, E.J. Nelson, and P. Pianetta, Phys. Rev. Lett. **84**, 773 (2000).

J.C. Woicik and E.J. Nelson